



# Immobilization of uranium(VI) by niobate/titanate nanoflakes heterojunction through combined adsorption and solar-light-driven photocatalytic reduction



Xiaona Liu<sup>a,b</sup>, Penghui Du<sup>c</sup>, Weiyi Pan<sup>d</sup>, Chenyuan Dang<sup>c</sup>, Tianwei Qian<sup>a</sup>, Hongfang Liu<sup>a</sup>, Wen Liu<sup>c,\*\*\*</sup>, Dongye Zhao<sup>a,b,\*</sup>

<sup>a</sup> Institute of Environmental Science, Taiyuan University of Science and Technology, Taiyuan, Shanxi 030024, PR China

<sup>b</sup> Environmental Engineering Program, Department of Civil Engineering, Auburn University, Auburn, AL 36849, United States

<sup>c</sup> The Key Laboratory of Water and Sediment Sciences, Ministry of Education, College of Environmental Sciences and Engineering, Peking University, Beijing 100871, PR China

<sup>d</sup> Department of Energy, Environmental, and Chemical Engineering, Washington University, St. Louis, MO 63130, United States

## ARTICLE INFO

**Keywords:**  
Titanate  
Niobate  
Radionuclide  
Adsorption  
Photocatalytic reduction

## ABSTRACT

A niobate/titanate nanoflakes (Nb/TiNFs) composite was synthesized through a one-step hydrothermal method. Nb/TiNFs displayed a heterojunction structure owing to deposition of a small fraction of niobate onto tri-titanate nanoflakes. Tri-titanate ( $\text{Na}_{1.6}\text{H}_{0.4}\text{Ti}_3\text{O}_7 \cdot 1.7\text{H}_2\text{O}$ ) was the primary crystal phase, and the molar ratio of niobate ( $\text{Na}_2\text{Nb}_2\text{O}_6 \cdot \text{H}_2\text{O}$ ) to titanate was determined to be 1:15.9. Nb/TiNFs showed rapid adsorption kinetics and high adsorption capacity for U(VI) (Langmuir  $Q_{\max} = 298.5 \text{ mg/g}$ ). Ion-exchange and surface complexation were the key mechanisms for U(VI) uptake, and the adsorption was further enhanced by the unique tunnel lattice structure of the heterojunction. Moreover, Nb/TiNFs were able to convert U(VI) into its immobile form,  $\text{UO}_2(\text{s})$  under solar light through photocatalytic reduction. More than 89.3% of (VI) was transformed into U(IV) after 4 h of solar irradiation (initial U(VI) = 20 mg/L, pH = 5.0). Diffuse reflectance UV-vis absorption spectra and Mott-Schottky plots indicated a narrowed band gap energy of Nb/TiNFs compared to neat TNTs. Density functional theory (DFT) calculation on band structure and density of states further confirmed the heterojunction architecture of niobate and titanate, resulting in offset of the conduction bands for the two phases in the composite material. Therefore, transfer of photo-excited electrons from titanate to niobate leads to inhibition of recombination of the electron-hole pairs. In addition, the trapping of uranium in the tunnel lattice of titanate and niobate heterojunction prevents re-oxidation of U(IV) to U(VI), thus achieving long-term immobilization of uranium. Remobilization tests indicated that only 18.7% of U(VI) was re-oxidized to U(VI) and almost no U dissolved into the aqueous phase when exposed air for 90 days. The new material is promising for separation and safe disposal of high strength radionuclides in water.

## 1. Introduction

Uranium (U) is a common radionuclide in soil and groundwater associated with nuclear materials mining, nuclear energy, nuclear weapon testing, and radioactive material disposal [1].  $^{238}\text{U}$  is the primary uranium isotope, which has a half-life of  $4.5 \times 10^9$  years [2]. Uranium has been known to pose widespread and lingering threat to the eco-systems and human health due to its radioactivity and carcinogenic effect [3,4].

The environmental fate and mobility of U is strongly related to its speciation and redox conditions of the matrix [1,5]. Under typical

environmental conditions, U(VI) and U(IV) are the most predominant species. U(VI), usually existing as  $\text{UO}_2^{2+}$  cations, is soluble and much more mobile in the environment, and thus is more likely to invade into the food chain [5,6]. In contrast, U(IV), mainly as  $\text{UO}_2$ , is only sparingly soluble ( $K_{\text{sp}} = -52.0$ ) and much less mobile [7], and thus is less likely to reach the food web [6,8]. Although adsorption has been widely studied for removal of U(VI) in contaminated water for its simplicity [9–12], reductive transformation of U(VI) to U(IV) precipitate is considered more viable as the reduced form of U(IV) is much more resistant to remobilization than the adsorbed U(VI). To this end, zero-valent iron and iron sulfide (FeS) have been the most studied materials for

\* Corresponding author at: Environmental Engineering Program, Department of Civil Engineering, Auburn University, Auburn, AL 36849, United States.

\*\* Corresponding author at: College of Environmental Sciences and Engineering, Peking University, Beijing 100871, PR China

E-mail addresses: [wen.liu@pku.edu.cn](mailto:wen.liu@pku.edu.cn) (W. Liu), [zhaodon@auburn.edu](mailto:zhaodon@auburn.edu), [dzhao@eng.auburn.edu](mailto:dzhao@eng.auburn.edu) (D. Zhao).

reductive immobilization of U(VI) [13–19].

Photocatalytic reduction is a promising technique considering its high efficiency, reusability of photocatalysts, no reducing agent consumption, low energy input if solar light is used, and environment-friendliness. However, photocatalytic transformation of U(VI) to U(IV) is hard to occur under normal oxic environmental conditions due to the low redox potential (0.411 V) of  $\text{UO}_2^{2+}/\text{UO}_2$  [20–22], where U(IV) can be easily re-oxidized to U(VI). Therefore, various photocatalysts, such as  $\text{TiO}_2/\text{Fe}_3\text{O}_4$  composite and sulfur doped g-C<sub>3</sub>N<sub>4</sub> [23,24], were developed to enhance the photo-reduction under specific conditions.

In recent years, titanate nanomaterials, especially titanate nanotubes (TNTs), have drawn great research interests due to their uniform structure in nanoscale, good ion-exchange property, surface and interface effect, and quantum size effect [25,26]. Both TNTs and titanate nanowires were reported to offer effective adsorption for U(VI) [12,27–29]. Moreover, metal-doped/deposited titanate or titanate composites have been shown to be highly effective photo-catalysts under visible/solar light [30–32]. Therefore, titanate may be used as a primary material for synthesizing new photocatalysts, which can combine the excellent ion-exchange/adsorption capacity and solar-light-driven photocatalytic activity upon proper tailoring of the material. Niobate exhibits similar ion-exchange properties to titanate, and has been shown to be effective adsorbents for radionuclides [33,34]. Moreover, incorporation of niobium or niobate into titanate may lead to a new electron donor level (valence band) and a heterojunction structure, which can enhance the photocatalytic activity in the visible light range [35,36]. Therefore, there is a great application potential of niobate/titanate heterojunction composite for photo-transformation of U(VI) to U(IV).

In this study, a new titanate niobate nanocomposite (Nb/TiNFs) with a heterojunction structure was synthesized, and tested for immobilization of <sup>238</sup>U(VI) through initial adsorption and subsequent photocatalytic reduction. The main objectives of this study were to: 1) develop a novel nanocomposite with titanate as the primary material and niobate as a photo-reaction facilitator; 2) test the U(VI) adsorption capacity and the photo-reduction efficiency by Nb/TiNFs under solar light; 3) elucidate the underlying adsorption mechanism and the effect of initial adsorption on subsequent photocatalysis; 4) explore the mechanisms on enhanced photocatalytic activity of the titanate niobate composite by means of computational chemistry analysis, and 5) test the re-oxidation and long-term stability of immobilized U.

## 2. Experimental

### 2.1. Chemicals

All chemicals used in this study were of analytical grade or higher. Nano-TiO<sub>2</sub> (P25, ~80% anatase and ~20% rutile) was obtained from Degussa (now Evonik) of Germany. NaOH, HCl, NaHCO<sub>3</sub>, Na<sub>2</sub>CO<sub>3</sub>, methanol (HPLC grade) and absolute ethanol were purchased from Acros Organics (Fair Lawn, NJ, USA). Nb<sub>2</sub>O<sub>5</sub> (99.5%) was acquired from Alfa Aesar of USA. Deionized (DI) water (Millipore Co., 18.2 MΩ cm) was used to prepare all solutions. A stock solution of U(VI) (1000 mg/L) was prepared by dissolving 2.11 g of  $\text{UO}_2(\text{NO}_3)_2 \cdot 6\text{H}_2\text{O}$  (International Bio-Analytical Industrial Inc., FL, USA, U in <sup>238</sup>U) in 1000 mL DI water.

### 2.2. Preparation and characterization of Nb/TiNFs

Nb/TiNFs were synthesized through a one-step hydrothermal treatment based on the method for TNTs preparation [37,38]. Typically, 1.2 g of TiO<sub>2</sub> and 0.1 g Nb<sub>2</sub>O<sub>5</sub> were mixed and dispersed into 80 mL of a 10 M NaOH solution. After magnetically stirred for 12 h, the mixture was transferred into a Teflon reactor with stainless steel coating, and allowed to react for 72 h at 130 °C. Afterwards, the white precipitate was washed with deionized water till pH ~9, and then

oven-dried at 105 °C for 4 h.

The material morphology was examined using a Tecnai30 FEG transmission electron microscopy (TEM, FEI, USA) operated at 300 kV. The crystal phase of the material was analyzed using a Dmax/2400 XRD (Rigaku, Japan) with Cu K $\alpha$  radiation ( $\lambda = 1.5418 \text{ \AA}$ ) and at a scan rate (20) of 4°/min. AXIS-Ultra X-ray photoelectron spectroscopy (XPS, Kratos, England) analysis was performed to determine the elemental compositions and oxidation states of Nb/TiNFs before and after reacting with U using Al K $\alpha$  X-ray at 15 kV and 15 mA. The standard C 1s peak (Binding energy,  $E_b = 284.80 \text{ eV}$ ) was used to eliminate the static charge effects. The Brunauer-Emmett-Teller (BET) surface area was measured on an ASAP 2010 BET surface area analyzer (Micromeritics, USA) in the relative pressure range of 0.06–0.20. Pore size distribution was obtained following the Barrett-Joyner-Halenda method. The nitrogen adsorption volume at the relative pressure of 0.99 was used to determine the pore volume and the average pore diameter. Diffuse reflectance UV-vis absorption spectra (UV-DRS) of the materials were obtained using a UV-2400 spectrophotometer (Shimadzu, Japan), and the band gap energy ( $E_g$ ) was calculated through the Kubelka-Munk function. The pH of point of zero charge (pH<sub>PZC</sub>) was obtained using a Nano-ZS90 Zetasizer (Malvern Instruments, UK) by measuring the zeta potentials at various pH values. The Mott-Schottky analysis method is described in Text S1 of the Supplementary Data.

### 2.3. Adsorption of U(VI) by Nb/TiNFs

Batch adsorption experiments were carried out in the dark and at room temperature (25 ± 0.5 °C) using 100 mL polyethylene bottles. In all cases, U solution was first purged with nitrogen (99.7%) for 1 h to remove dissolved oxygen. The kinetic tests were conducted at two levels of initial U(VI) concentrations (50 and 100 mg/L) and a Nb/TiNFs dosage of 0.2 g/L and solution pH of 5.0. The solution pH was adjusted by diluted HCl and NaOH. The reaction was initiated by adding 0.02 g of Nb/TiNFs into 100 mL of the deoxygenated U(VI) solution. The mixture was then shaken at 200 rpm and the adsorption rate was followed for 360 min. Samples were taken at predetermined time intervals and immediately filtered through a 0.22 μm polyethersulfone (PES) membrane, and U(VI) concentration in the filtrate was determined on an inductively coupled plasma-optical emission spectroscopy (ICP-OES, 710-ES, Varian, USA). Isotherm tests were carried out in a similar manner, where 0.2 g/L of Nb/TiNFs was mixed with U(VI) solutions at a range of initial concentrations (10–200 mg/L) and at pH 5.0. The mixtures were equilibrated under shaking for 240 min to reach adsorption equilibrium. Control tests indicated no adsorption loss of U(VI) by the bottles and the membrane filtration.

The equilibrium U(VI) uptake ( $q_e$ , mg/g) and removal efficiency ( $R$ , %) are calculated by:

$$q_e = \frac{(C_0 - C_e)V}{m} \quad (1)$$

$$R = \frac{C_0 - C_e}{C_0} \times 100\% \quad (2)$$

where  $C_0$  and  $C_e$  (mg/L) are the initial and equilibrium concentrations of U(VI) in the aqueous phase, respectively;  $V$  (L) is the solution volume and  $m$  (g) is the mass of Nb/TiNFs.

### 2.4. Photocatalytic reduction of U(VI) by Nb/TiNFs under simulated solar light

Batch photocatalytic reduction experiments were conducted in a sealed glass photo-reactor (volume = 250 mL) with a quartz cover (Fig. S1 in Supplementary Data). Cooling water was circulated around the reactor to maintain the system temperature of (25 ± 0.2 °C). An Oriel Sol 1A solar simulator (Newport, USA) with a 450 W xenon lamp was used as the source of solar light, which has a light intensity in the

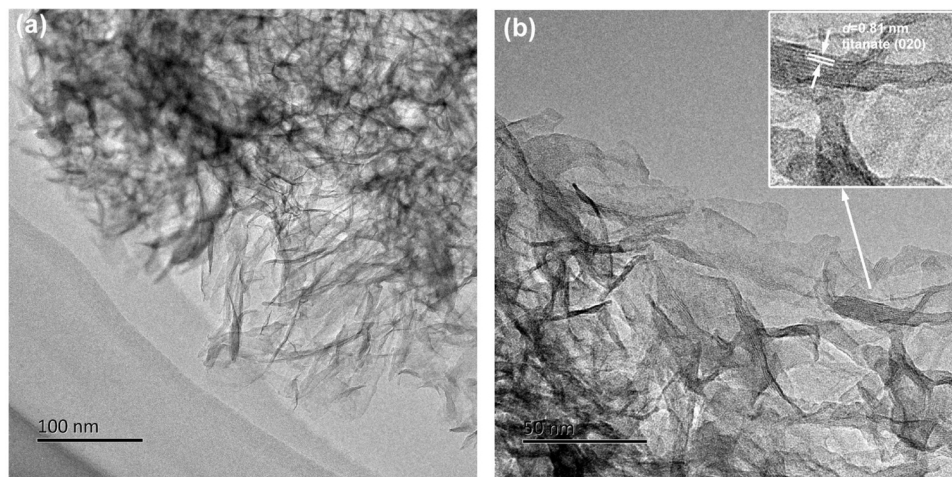


Fig. 1. (a) TEM and (b) high resolution TEM (HRTEM) images of Nb/TiNFs.

reaction center of  $85 \pm 0.5 \text{ mW/cm}^2$  (AM 1.5G). A UV cut-off filter (Beijing Electric Light Institute, China) was used to remove the UV light with wavelengths  $< 420 \text{ nm}$  so as to examine the contribution of visible light to the U(VI) photo-reduction.

In each test, 100 mL of U(VI) solution ( $C_0 = 20$  or 50 mg/L) was loaded and then purged with nitrogen for 1 h to ensure the adsorption and photocatalysis proceed under anoxic conditions. Afterwards, adsorption was first initiated by adding 0.2 g/L of Nb/TiNFs into the solution (pH adjusted to 5.0). The adsorption lasted for 3 h in the dark (without photocatalytic reaction) under gentle mixing. Subsequently, the mixture was subjected to the solar irradiation, and the photocatalytic reaction was followed for 4 h by analyzing U(VI) in both of the aqueous and solid phases. During the tests, 2 mL methanol (2% v/v) was added into the solution to quench the hole during the reaction [24]. A widely used anoxic carbonate (CARB) extraction method was used to extract adsorbed U(VI) after the photo-reduction [39,40]. Specifically, the suspension after reaction was transferred to poly-propene (PP) centrifuge tubes sealed with Teflon-lined caps. The material was first separated from the solution via centrifugation (8000 rpm, 5 min), and then the supernatant was replaced by 50 mL of the extracting solution consisting of sodium bicarbonate (14.4 mM) and sodium carbonate (2.8 mM) under  $\text{N}_2$  atmosphere. The mixture was then vortexed for a minute and then allowed to react for 1 h on an end-over-end rotator. Upon filtration through a  $0.22 \mu\text{m}$  PES membrane, U(VI) in the extractant was measured on ICP-OES. Consequently, U(IV), which is not CARB-extractable, was quantified per mass balance calculations. To probe pH effects, the adsorption and photo-reduction experiments were also carried out in the broad pH range from 3.0 to 11.0.

## 2.5. DFT calculations

For sodium titanate (use a typical chemical structure of  $\text{Na}_2\text{Ti}_3\text{O}_7$ ) and orthorhombic sodium niobate (a chemical structure of  $\text{Na}_2\text{Nb}_2\text{O}_6$ ), the first-principle calculations were performed using the CASTEP package provided by Material Studio 7, with the plane-wave-based pseudopotential method within density functional theory (DFT) [41]. For  $\text{Na}_2\text{Ti}_3\text{O}_7$ , the generalized gradient approximation with the Perdew-Bueke-Ernzerh (GGA-PBE) approximation for the exchange-correlation function was employed [42]. The interaction between ion cores and the electrons were represented by the Vanderbilt-type ultrasoft pseudopotentials [43]. The plane wave cut-off energy was 340 eV. The reciprocal-space integration over the Brillouin zone was carried out by using the Monkhorst-Pack scheme with a  $2 \times 5 \times 2$   $k$ -sampling in the irreducible wedge. For  $\text{Na}_2\text{Nb}_2\text{O}_6$ , the core electrons were replaced by ultrasoft pseudopotentials with a 370 eV plane-wave basis cutoff energy. The frame work of local density approximation (LDA) was applied

to treat the interactions of exchange and correlation. The fast-Fourier-transform (FFT) grids of basis and the  $k$ -point sets were  $32 \times 90 \times 90$  and  $5 \times 2 \times 5$ , respectively [44].

## 2.6. Re-oxidation and stability of photo-immobilized U(IV)

Following the adsorption-photocatalytic reduction tests (20 mg/L U (VI) with 0.2 g Nb/TiNFs at pH 5.0) described in Section 2.4, selected batches of the particle-solution mixtures were transferred into 100 mL plastic bottles. To probe the stability and re-oxidation potential of the photo-immobilized U, the aqueous phase concentration of U was then monitored for 90 days under oxic conditions (with the bottles being open to air). The U dissolution was measured by following the concentration history of U in the aqueous phase, whereas CARB extractions were also exercised to determine the production of U(VI) in the solid phase through re-oxidation. At 90 d, the U-loaded Nb/TiNFs was separated and dried in a nitrogen ( $> 99.7\%$ ) atmosphere, and then immediately subjected to the XPS analysis to test the oxidation state of U in the solid phase.

## 3. Results and discussion

### 3.1. Morphology, crystal phase and compositions of Nb/TiNFs

Fig. 1 displays the TEM images of Nb/TiNFs. Unlike the tubular structure of TNTs (Fig. S2), which are synthesized under the same conditions but without addition of Nb [32,45,46], Nb/TiNFs appear as nanoflakes (Fig. 1). In addition, the nanoflakes display a crystalline interlayer distance of 0.81 nm (Fig. 1b), which is consistent with the crystal plane of sodium titanate (200) [37,47]. These curved titanate nanosheets may be envisioned as a transition state from nanosheets to nanotubes as in TNTs [37,48,49]. Evidently, the addition of a small fraction of Nb (in the form of  $\text{Nb}_2\text{O}_5$ ) as a co-precursor in the hydro-thermal treatment affected the morphology and structure of the resulting composite material.

Fig. 2 shows the XRD patterns of various titanium and niobium materials. The titanium precursor,  $\text{TiO}_2$  P25, is composed of anatase and rutile; and the  $\text{Nb}_2\text{O}_5$  powders contain a hexagonal (PDF#07-0061) phase and a monoclinic (PDF#19-0862) phase. For the neat material, the peak at ca. 9.3° indicates the interlayer distance of Nb/TiNFs [45]. The primary diffractions at 24.5°, 28.5°, 48.1° and 62.0° are assigned to sodium titanate, which can be represented by the chemical formula  $\text{Na}_x\text{H}_{2-x}\text{Ti}_3\text{O}_7 \cdot n\text{H}_2\text{O}$  ( $x$  depends on the sodium content) [45,50]. Therefore, the titanate nanoflakes are composed of tri-titanate, with layered corrugated ribbons resulting from edge-sharing of triple  $[\text{TiO}_6]$  octahedrons (the skeleton) and the exchangeable  $\text{H}^+$ / $\text{Na}^+$  ions located

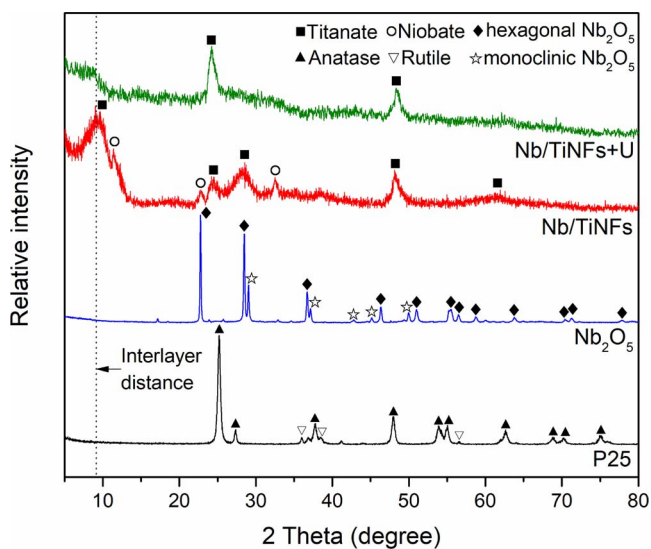


Fig. 2. XRD patterns of precursors and synthesized Nb/TiNFs composite.

in the interlayers [45,49–51]. The weak peaks at 11.4°, 22.8° and 32.5° are in accordance with the crystal planes of (200), (110) and (510) of sodium niobate, respectively [33,34]. The sodium niobate accords with a chemical formula of  $\text{Na}_2\text{Nb}_2\text{O}_6 \cdot \text{H}_2\text{O}$ , comprising a tunnel structure with a framework formed by the edge sharing of  $[\text{NbO}_6]$  and  $[\text{NaO}_6]$  octahedrons and with exchangeable  $\text{Na}^+$  ions in the channels [52]. Therefore, Nb/TiNFs are a composite material of titanate and niobate, with tri-titanate being the main crystal phase.

Fig. 3 shows the XPS spectra of Nb/TiNFs before and after adsorption/photo-reaction with U(VI) loaded solutions, and Table 1 lists the elemental compositions of the materials. The main elements of neat Nb/TiNFs are Na (12.1 at.-%), O (65.5 at.-%), Ti (21.5 at.-%) and Nb (0.9 at.-%) (Fig. 3a and Table 1). Apparently, the hydrothermal reaction (130 °C for 72 h) in the material synthesis resulted in a much higher yield of titanate than that of niobate. Based on the atomic ratios of the elements, the synthesized Nb/TiNFs can be described as  $[\text{Na}_2\text{Nb}_2\text{O}_6 \cdot \text{H}_2\text{O}] / 15.9[\text{Na}_{1.6}\text{H}_{0.4}\text{Ti}_3\text{O}_7 \cdot 1.7\text{H}_2\text{O}]$ , where “ $\text{Na}_2\text{Nb}_2\text{O}_6 \cdot \text{H}_2\text{O}$ ” represents sodium niobate and “ $\text{Na}_{1.6}\text{H}_{0.4}\text{Ti}_3\text{O}_7 \cdot 1.7\text{H}_2\text{O}$ ” sodium titanate. The Na content in Nb/TiNFs was calculated to be 4.96 mmol/g based on the XPS analysis, which is higher than that of 3.33 mol/g in neat TNTs, suggesting abundant  $-\text{ONa}$  groups located in the material [12,53,54]. Previous studies indicated that  $-\text{ONa}$  groups are the primary active sites of titanate materials for metal cations adsorption, and the Na content governs the adsorption capacity [53,54].

The BET surface area of Nb/TiNFs was measured to be 146.6 m<sup>2</sup>/g (Fig. S3), which is 46% smaller than that of TNTs (272.3 m<sup>2</sup>/g) [46], which is consistent with the titanate nanoflake structure of Nb/TiNFs and the tubular structure of TNTs, and it confirms the role of Nb in altering the structure of titanate. The  $\text{N}_2$  adsorption-desorption isotherms for Nb/TiNFs are consistent with type IV isotherms with H3 hysteresis loops according to the classical BDDT classification and the 2015 IUPAC definition [55,56], suggesting the presence of mesopores (2–50 nm) in the material (Fig. S3) [57]. The bimodal pore size distribution further confirms the mesoporous structure of Nb/TiNFs (Fig. S4): the smaller pores with a peak diameter of ~3–4 nm are assigned to the internal space of curly nanoflakes or space between crossed titanate and niobate, while the larger pores with a peak diameter of ~5–6 nm are attributed to the gaps between the nanoflakes and voids in the aggregates of the primary clusters [58,59]. The  $\text{pH}_{\text{PZC}}$  of Nb/TiNFs was measured to be 2.61 (Fig. S5), predicting a rather negatively charged material surface due to the fixed  $\text{O}^-$  functionalities in the broad pH range. The high Na content, large specific surface area and low  $\text{pH}_{\text{PZC}}$  of Nb/TiNFs are all conducive to adsorption of U(VI) cations.

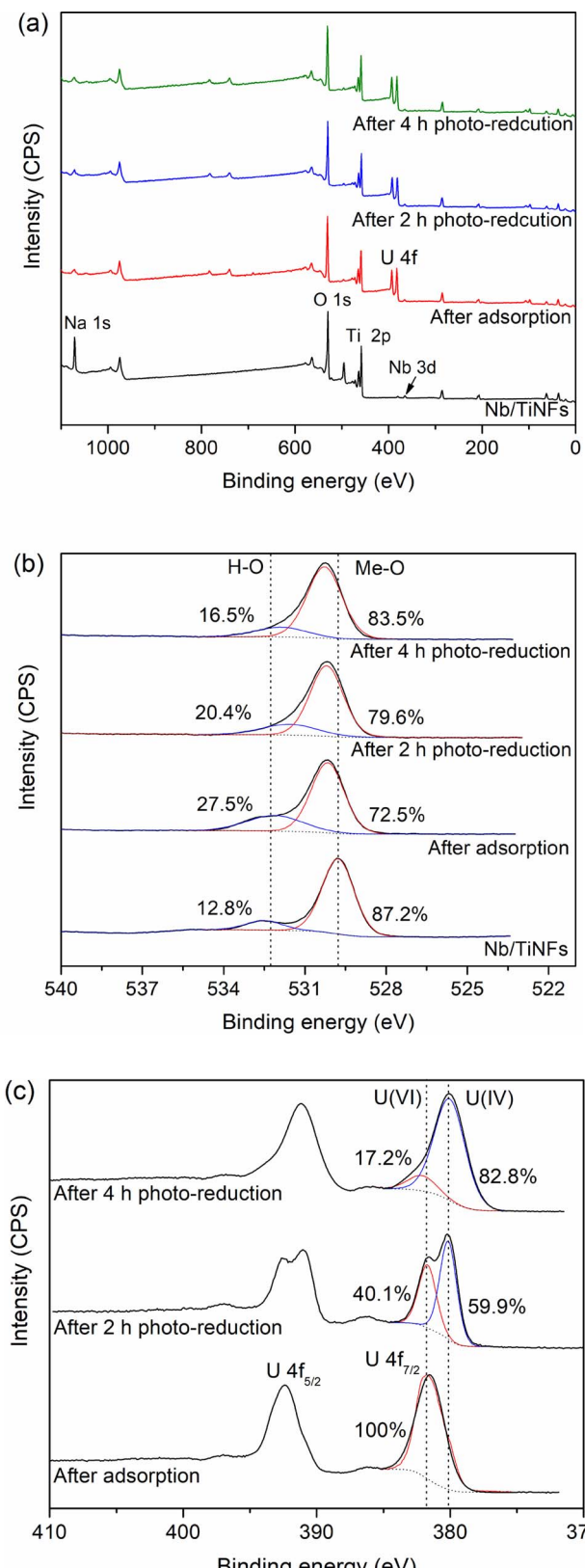


Fig. 3. XPS spectra of neat and reacted Nb/TiNFs. (a) Survey spectra, (b) high resolution spectra of O 1s, and (c) high resolution spectra of U 4f.

### 3.2. Adsorption kinetics and isotherms of U(VI) by Nb/TiNFs

Adsorption of U(VI) by Nb/TiNFs without photo-reduction was first investigated. Fig. 4a shows adsorption kinetics of U(VI) at an initial

**Table 1**

Atomic percentiles of various elements in Nb/TiNFs before and after adsorption and photo-reduction of U(VI).

Material	Elements (at.%)				
	Na	O	Ti	Nb	U
Nb/TiNFs	12.1	65.5	21.5	0.9	0.0
After adsorption	3.8	74.0	20.1	0.8	1.3
After 2 h photo-reduction	3.7	73.4	20.5	0.9	1.5
After 4 h photo-reduction	3.6	72.1	21.8	0.9	1.6

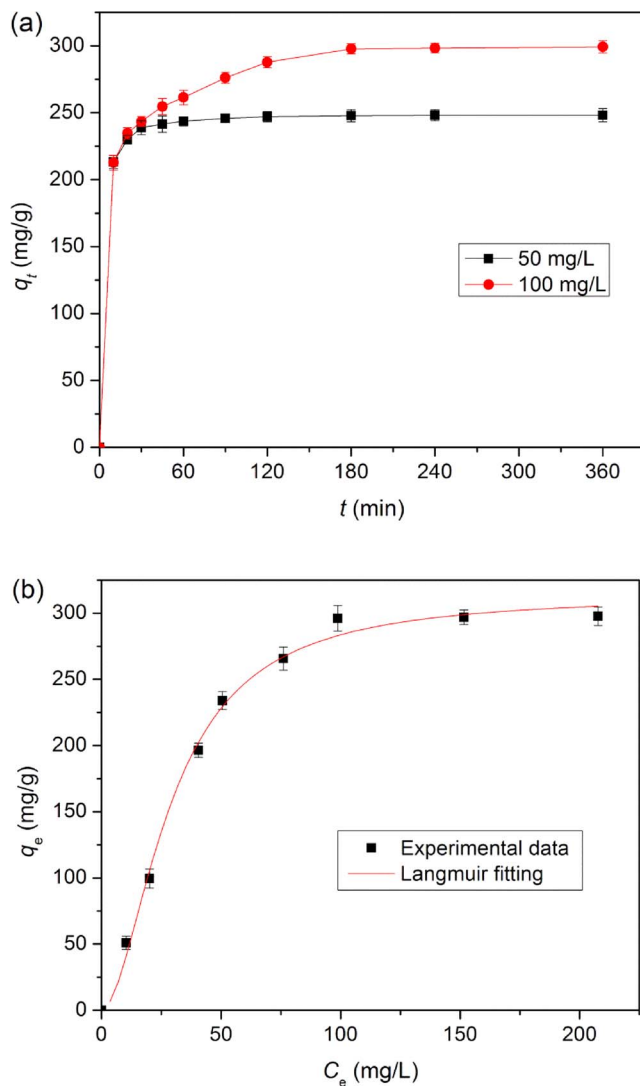


Fig. 4. Adsorption kinetics (a) and isotherms (b) of U(VI) by Nb/TiNFs. Experimental conditions: material dosage = 0.2 g/L, pH = 5.0 ± 0.1; for (a), initial U(VI) = 50 or 100 mg/L, and for (b), initial U(VI) = 0 – 200 mg/L.

concentration of 50 and 100 mg/L. It is evident that Nb/TiNFs were able to rapidly adsorb U(VI) ions from solution. The rapid adsorption rate can be attributed to the flaky sheet structure of Nb/TiNFs, which allows for fast mass transfer and easy access to the ion exchange sites, and the large specific surface area of the material [12,33,34]. The most U(VI) uptake occurred in the initial 30 min, and the adsorption equilibrium was reached within 120 min ( $C_0 = 50$  mg/L) and 180 min ( $C_0 = 100$  mg/L). The equilibrium U(VI) removal reached 92.7% with a high equilibrium uptake ( $q_e$ ) of 231.7 mg/g for the case of  $C_0 = 50$  mg/L, and 59.8% ( $q_e = 299.2$  mg/g) for  $C_0 = 100$  mg/L.

The pseudo-first (Eq. (3)) and pseudo-second order (Eq. (4)) kinetic

models are used to interpret the adsorption kinetic data [60,61]:

$$q_t = q_e - q_e \exp(-k_1 t) \quad (3)$$

$$\frac{t}{q_t} = \frac{1}{k_2 q_e^2} + \frac{t}{q_e} \quad (4)$$

where  $q_t$  and  $q_e$  (mg/g) are the U(VI) uptakes at time  $t$  (min) and equilibrium, respectively, and  $k_1$  (min<sup>-1</sup>) and  $k_2$  (g/(mg·min)) are the respective rate constants.

Table S1 lists the best-fitted kinetic model parameters. It is evident that the pseudo-second order model better describes the kinetic data ( $R^2 > 0.999$ ). In addition, the pseudo-second order model much better simulated equilibrium U(VI) uptakes (deviation < 2%). The model fitting also suggests that the rate-controlling step for U(VI) adsorption onto Nb/TiNFs is likely to be the surface interactions between the –ONa groups of Nb/TiNFs and U(VI) cations, i.e., ion exchange between interlayered Na<sup>+</sup> with U(VI) cations and surface complexation [12,53].

The classical Langmuir (Eq. (5)) and Freundlich (Eq. (6)) isotherm models are used to interpret the adsorption isotherm data (Fig. 4b) [62,63]:

$$q_e = \frac{Q_{\max} b C_e}{1 + b C_e} \quad (5)$$

$$q_e = K_F C_e^{1/n} \quad (6)$$

where  $C_e$  (mg/L) is the equilibrium concentration of U(VI) in the aqueous phase,  $Q_{\max}$  (mg/g) is the maximum Langmuir adsorption capacity, and  $b$  (L/mg) is the Langmuir constant related to the affinity of binding sites and is also a measure of free energy of adsorption.  $K_F$  ((mg/g)·(L/mg)<sup>1/n</sup>) is the Freundlich constant related to the adsorption capacity of the adsorbent, and  $n$  is the heterogeneity factor indicating the adsorbent intensity of the adsorbent.

Based on the Langmuir model, a dimensionless constant termed separation factor ( $R_L$ ) is used to evaluate the adsorption affinity [64]:

$$R_L = \frac{1}{1 + b C_0} \quad (7)$$

where  $C_0$  (mg/L) is the initial concentration of U(VI) in solution. Accordingly, the adsorption can be classified as irreversible ( $R_L = 0$ ), favorable ( $0 < R_L < 1$ ), linear ( $R_L = 1$ ) and unfavorable ( $R_L > 1$ ).

Table S2 lists the simulated isotherm model parameters. The Langmuir model offered much better fitting ( $R^2 = 0.9997$ ) than the Freundlich model, with a  $Q_{\max}$  of 298.5 mg/g, which agrees with the uniform, monolayer ion exchange and surface complexation mechanism, and suggests there is no interaction between the adsorbed  $\text{UO}_2^{2+}$  ions [62]. The relatively low  $R_L$  values, 0.014 for  $C_0 = 50$  mg/L and 0.007 for  $C_0 = 100$  mg/L, indicate very favorable adsorption of U(VI) by Nb/TiNFs. It is noteworthy that the simulated  $Q_{\max}$  (298.5 mg/g) of Nb/TiNFs is slightly lower than that of TNTs (333 mg/g), which is consistent with its flake structure and smaller specific surface area [12]. However, the U(VI) adsorption capacity of Nb/TiNFs is still much higher than many other adsorbents reported, such as activated carbon (58.4 mg/g) [65], talc (41.6 mg/g) [66], sepiolite (18.47 mg/g) [67], manganese oxide coated zeolite (15.1 mg/g) [9], graphene oxides (138.9 mg/g) [68], and graphene oxide/polypyrrole (147.1 mg/g) [69].

### 3.3. Photocatalytic reduction of U(VI) by Nb/TiNFs

Fig. 5 displays the U(VI) reduction and U(IV) formation rates during the adsorption-photocatalysis. For comparison, photocatalysis of U(VI) by neat TNTs prepared without Nb under solar light was also tested. Fig. S6 shows that removal of less than 2% U(VI) was photo-reduced in the presence of the neat TNTs under solar light, i.e., nearly all U(VI) removal was due to adsorption for neat TNTs. This is consistent with the previous studies that such neat titanate based photocatalysts are not

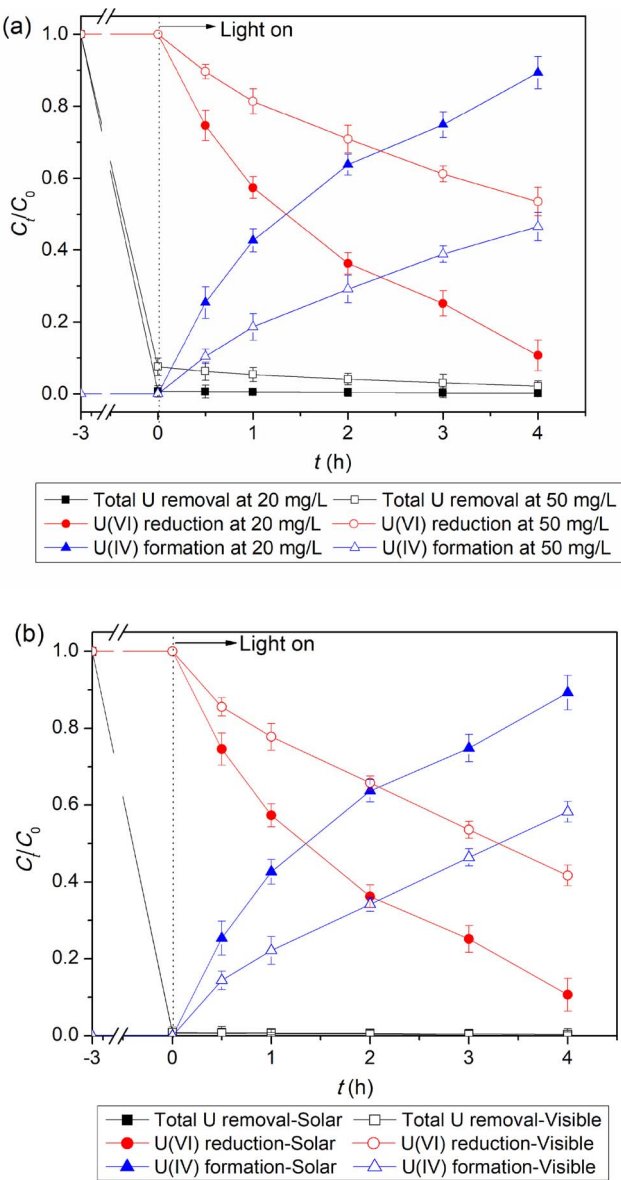


Fig. 5. Reduction of U(VI), formation of U(IV) and overall removal of U by Nb/TiNFs during adsorption and subsequent photo-catalytic reduction processes. Experimental conditions: material dosage = 0.2 g/L, pH = 5.0 ± 0.1; For (a), initial U(VI) = 20 or 50 mg/L, solar light intensity = 85 ± 0.5 mW/cm<sup>2</sup>; For (b), initial U(VI) = 20 mg/L, under solar and visible light sources.

effective for photocatalytic reduction of U(VI) under solar lights [20,21], which can be attributed to: (1) the weak photocatalytic property of titanate due to immediate re-combination of electron-hole pairs after excitation [31,32], and (2) quick re-oxidation of U(IV) to U(VI) in the photocatalysis process [20,21].

In contrast, Nb/TiNFs were able to facilitate highly effective photocatalytic reduction of U(VI) to U(IV) (Fig. 5). The initial adsorption removed 99.5% ( $C_0 = 20$  mg/L) and 92.5% ( $C_0 = 50$  mg/L) the soluble U(VI) by Nb/TiNFs (within the first 3 h). The CARB extraction indicated that no reduction of U(VI) occurred when the light was absent. However, under the solar light irradiation, rapid photocatalytic reduction of U(VI) was observed. After 4-h irradiation, Nb/TiNFs converted 89.3% ( $C_0 = 20$  mg/L) and 46.5% ( $C_0 = 50$  mg/L) of U(VI) into U(IV) (Fig. 5).

The pseudo-first order kinetic model is used to interpret the kinetic data on photo-reduction of U(VI) [46,70]:

$$\ln(q_0/q_t) = k_1 t \quad (8)$$

where  $q_0$  and  $q_t$  (mg/L) are the U(VI) concentrations in the solid phase (material) at time zero and  $t$  (h), respectively, and  $k_1$  (h<sup>-1</sup>) is the first-order rate constant.

The model can well describe the photocatalytic reduction kinetics of U(VI) to U(IV) ( $R^2 > 0.98$ ) (Table S3), and the best-fitted  $k_1$  was 0.518 h<sup>-1</sup> for  $C_0 = 20$  mg/L and 0.163 h<sup>-1</sup> for  $C_0 = 50$  mg/L. Moreover, the photocatalytic conversion promoted further removal of total U from the aqueous phase, with a final total U removal efficiency of 99.9% ( $C_0 = 20$  mg/L) and 97.9% ( $C_0 = 50$  mg/L). Apparently, the photo-transformation of  $\text{UO}_2^{2+}$  into neutral  $\text{UO}_2$  precipitates freed up some ion exchange sites on Nb/TiNFs, resulting in enhanced adsorption of U(VI). Overall, U(VI) cations were first adsorbed on the lattice structure of Nb/TiNFs, and then transformed into U(IV) via photocatalysis, leading to precipitation of  $\text{UO}_2$  in the lattice, which is expected to be very stable because of the steric hindrance and shielding effects from re-oxidation (See Section 3.5) [33,67].

Fig. 5b shows photocatalytic reduction kinetics of U(VI) ( $C_0 = 20$  mg/L) by Nb/TiNFs under solar and visible light sources. In both cases, U was rapidly and nearly completely removed from the aqueous phase. However, the photo-reduction rate of U(VI) was decreased when the UV light was cut off, and the percentage of (IV) formed was decreased from 88.2% to 58.8% in the end of the experiment, and the  $k_1$  value was decreased from 0.518 to 0.216 h<sup>-1</sup> (Table S3), with the difference being attributed to the UV portion (wavelength < 420 nm) of sunlight. Evidently, both visible and UV lights play important roles in the photo-reduction of U(VI). The results are in accordance with previous studies, which confirmed that titanate-based materials generally show good UV response [25,26,71,72]. However, in this study, the deposition of niobate on titanate leads to the heterojunction structure of Nb/TiNFs, thus greatly promoting the visible-light-driven photocatalytic activity (see detailed discussion in Section 3.4). From a practical application standpoint, solar light is a much preferred light source compared to UV for its cost-effectiveness and “greenness”, and thus, Nb/TiNFs offers some unparalleled advantages over conventional titanate-based materials.

Fig. 6 shows effects of pH on the adsorption (in dark) and U(VI) photo-reduction (under solar light) of U(VI) by Nb/TiNFs. Increasing pH from 4.0 to 5.0 remarkably increased the adsorption of U(VI) from 64.4% to 99.3%. This is in accord with the trend that the surface potential, as indicated by the zeta potential (Fig. S5), became more negative at higher pH and more ion exchange sites become available due to increased deprotonation, which favors the uptake of various U(VI) cationic species, including  $\text{UO}_2^{2+}$ ,  $(\text{UO}_2)_2(\text{OH})_2^{2+}$ ,  $(\text{UO}_2)_3(\text{OH})_5^+$  and

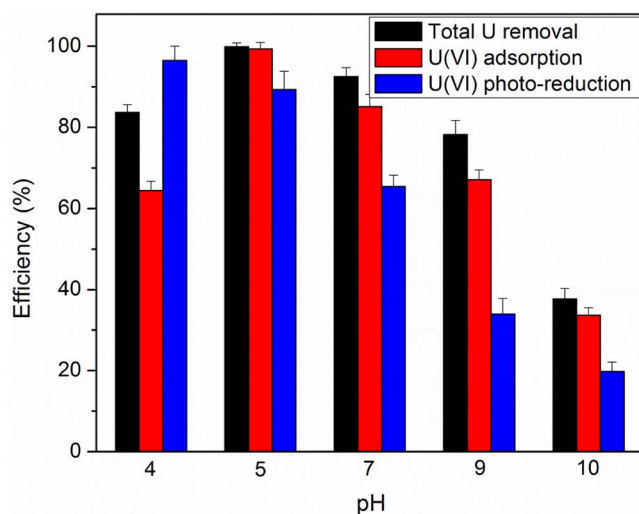


Fig. 6. Effect of pH on U(VI) adsorption and photo-reduction by Nb/TiNFs. Experimental conditions: initial U(VI) = 20 mg/L, material dosage = 0.2 g/L, solar light intensity = 85 ± 0.5 mW/cm<sup>2</sup>.

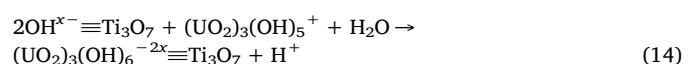
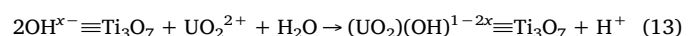
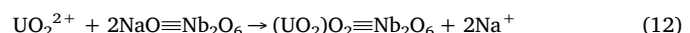
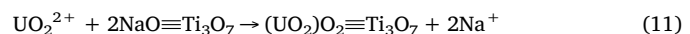
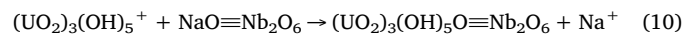
$(\text{UO}_2)_4(\text{OH})_7^+$  (Fig. S7). However, it appears that the surface charge (or ion pairing) alone may not fully account for the rather remarkable increase in the U(VI) uptake. Comarmond et al. [73] studied U sorption on various forms of titanium dioxide, and reported that differences in sorption properties between the various  $\text{TiO}_2$  materials were more related to the crystallographic form, morphology, surface area, and grain size, rather than to surface charge. Therefore, surface complexation is playing an important role as well in addition to the electrostatic interactions and ion exchange in the adsorption of U(VI) by titanate. Generally, there are two types of U(VI) surface complexes can be formed upon reacting with  $[\text{TiO}_6]$  octahedrons [74]: one results from sorption of  $\text{UO}_2^{2+}$  ions on the two bridging oxygen atoms of  $[\text{TiO}_6]$ , and the other, which is favored at higher surface coverages, is due to interactions with the one bridging oxygen atom and one top oxygen atom. Sylvester et al. [75] observed that adsorption of uranyl ions onto montmorillonite at low pH occurs via ion exchange, leaving the inner-sphere uranyl aquo-ion structure intact, but at near-neutral pH, inner-sphere complexation with the surface becomes predominated; furthermore, they claimed that adsorption of the uranyl onto silica and  $\gamma$ -alumina surfaces appeared to occur via inner-sphere, bidentate complexation, with the formation of polynuclear surface complexes at near-neutral pH. Based on EXAFS analysis, Singh et al. [76] observed that U (VI) is adsorbed on goethite via bidentate edge-sharing ( $(\equiv\text{Fe}(\text{OH})_2\text{UO}_2)$ ) and bidentate corner-sharing ( $(\equiv\text{FeOH})_2\text{UO}_2$ ) at pH 4–7, and the uptake mechanisms changed from adsorption to precipitation with increasing pH and U(VI) concentration. Based on these results, it appears that the increase in U(VI) uptake from pH 4.0 to 5.0 can be attributed to much enhanced surface complexation between the predominant U(VI) species ( $\text{UO}_2^{2+}$  and  $(\text{UO}_2)_3(\text{OH})_5^+$ ) and the titanate surfaces.

Further increasing pH to 7.0 diminished the adsorption of U(VI) to 92.5%, which is due to the lowered solubility of U(VI) at pH 7.0 and conversion of cationic U(VI) species into neutral uranyl molecules (e.g.,  $\text{UO}_2(\text{OH})_2$ ,  $(\text{UO}_2)_3(\text{OH})_6^-$  and  $(\text{UO}_2)_4(\text{OH})_8^-$ ) [12,77]. At pH  $\geq 9$ ,  $(\text{UO}_2)_3(\text{OH})_7^-$  and  $\text{UO}_2(\text{OH})_3^-$  became the predominant U species, which are subject to elevated Donnan co-ion exclusion effect, and thus the ion pairing process became exceedingly unfavorable [12,67].

For the photocatalytic reduction of U(VI) to U(IV), the acidic condition promoted the reaction as protons ( $\text{H}^+$ ) played an important role in the reaction (see more details in Section 3.4) [20]. When pH was increased from 4.0 to 10, the photocatalytic transformation efficiency of U(VI) to U(IV) decreased from 96.5% to 18.9%. The highest total U removal efficiency (99.9%) in the combined adsorption-photocatalysis process was found at pH 5.0. Evidently, both adsorption and photocatalysis are important for the overall removal of U(VI) by Nb/TiNFs. Adsorption plays a two-fold role: 1) it facilitates the photocatalytic reaction by initially concentrating U(VI) ions from the aqueous phase to vicinity of the photochemical reactive sites, and 2) a fraction of U(VI) is adsorbed on some sites that require a high desorption activation energy, thus directly immobilizing U(VI).

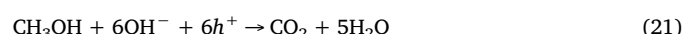
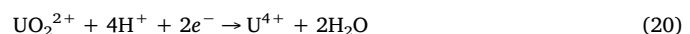
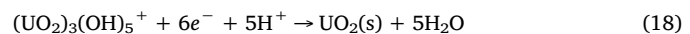
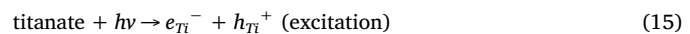
### 3.4. Adsorption and photocatalytic reduction mechanisms and DFT analysis

Adsorption of U(VI) at the experimental pH (5.0) is mainly attributed to ion-exchange between the uranyl cations and the exchangeable  $\text{Na}^+$  ions in the interlayers of sodium titanate and niobate composite [12,33,34]. In addition, inner sphere complexation further enhances the adsorption, which may occur between U(VI) and the bridging O atoms from  $[\text{TiO}_6]$  octahedrons of titanate, and/or  $[\text{NbO}_6]$  and  $[\text{NaO}_6]$  octahedrons of niobate [29,74]. Fig. 7a depicts the schematic of the ion exchange process occurring on sodium titanate and sodium niobate.  $(\text{UO}_2)_3(\text{OH})_5^+$  is the primary species of U(VI) at pH 5.0, followed by  $\text{UO}_2^{2+}$ ,  $(\text{UO}_2)_2(\text{OH})_2^{2+}$  and  $(\text{UO}_2)_4(\text{OH})_7^-$ . Taking  $(\text{UO}_2)_3(\text{OH})_5^+$  and  $\text{UO}_2^{2+}$  as examples, the ion-exchange and complexation processes can be described as follows [12,33,34,54]:



where “ $\text{NaO} \equiv \text{Ti}_3\text{O}_7$ ” and “ $\text{OH}^{x-} \equiv \text{Ti}_3\text{O}_7$ ” represent the functional group of titanate and “ $\text{NaO} \equiv \text{Nb}_2\text{O}_6$ ” denotes that of niobate.

Fig. 7b displays a conceptualized representation on the photocatalytic reduction of U(VI) by Nb/TiNFs. Under solar light irradiation, both of the titanate and niobate phases can be excited, leading to the formation of pairs of the conduction band (CB) and the valence band (VB) for both materials with different energy band gaps (Eqs. (15) and 16). Due to the Nb tailoring, the electrons generated on titanate (the primary photocatalyst) are transferred to the CB of niobate due to their conduction band offset (Eq. (17)), thus inhibiting recombination of electron-hole pairs. Consequently, more electrons become available for the reduction of U(VI) to U(IV) via Eqs. (18)–(20) [20]. Note that methanol was used to quench  $\text{h}^+$ , which also helps prevent recombination of the  $e^- - \text{h}^+$  pairs (Eq. (21)) [24].



Eqs. (18) and (20) indicate that the acidic condition facilitates photocatalytic reduction of U(VI), which is consistent with the results on pH effect (Fig. 6).

UV-DRS spectra (Fig. 8a) indicate that the light absorbance edge for Nb/TiNFs was shifted to the visible range of 451 nm (compared to 361 nm for TNTs). Meanwhile, the band gap energy of Nb/TiNFs was narrowed to 2.74 eV (compared to 3.42 eV for TNTs), indicating enhanced visible-light-driven photocatalytic activity after niobate deposition.

The CB energy level is further determined by measuring the flat-band potential ( $E_{fb}$ ), which was obtained from the extrapolation of the Mott-Schottky plots according to the following equation [78]:

$$C^{-2} = \frac{2}{N_D \epsilon_0 \epsilon e_0} \left( E - E_{fb} - \frac{k_B T}{e_0} \right) \quad (22)$$

where  $C$  is the space charge capacitance,  $E$  is the externally applied potential,  $E_{fb}$  is the flat-band potential at the semiconductor/electrolyte junction,  $N_D$  is the donor density,  $\epsilon_0$  is the permittivity of free space,  $\epsilon$  is dielectric constant of the semiconductor electrode,  $e$  is the elementary charge,  $k_B$  is Boltzmann's constant, and  $T$  is the operation temperature (298 K).

Fig. 8b displays the typical Mott-Schottky plots of TNTs and Nb/TiNFs electrodes. The positive slopes of the two lines suggest that both of the materials are  $n$ -type semiconductors, with a close  $E_{fb}$  value of  $-0.61$  V for TNTs and  $-0.62$  V for Nb/TiNFs, respectively. It is well known that the CB potential of  $n$ -type semiconductor is about 0.1 V more negative than  $E_{fb}$  [79]. The CB and VB energy levels of Nb/TiNFs are calculated to be  $-0.72$  V and  $2.02$  V (vs. SCE), respectively. Therefore, the potential energy of CB from Nb/TiNFs is more negative

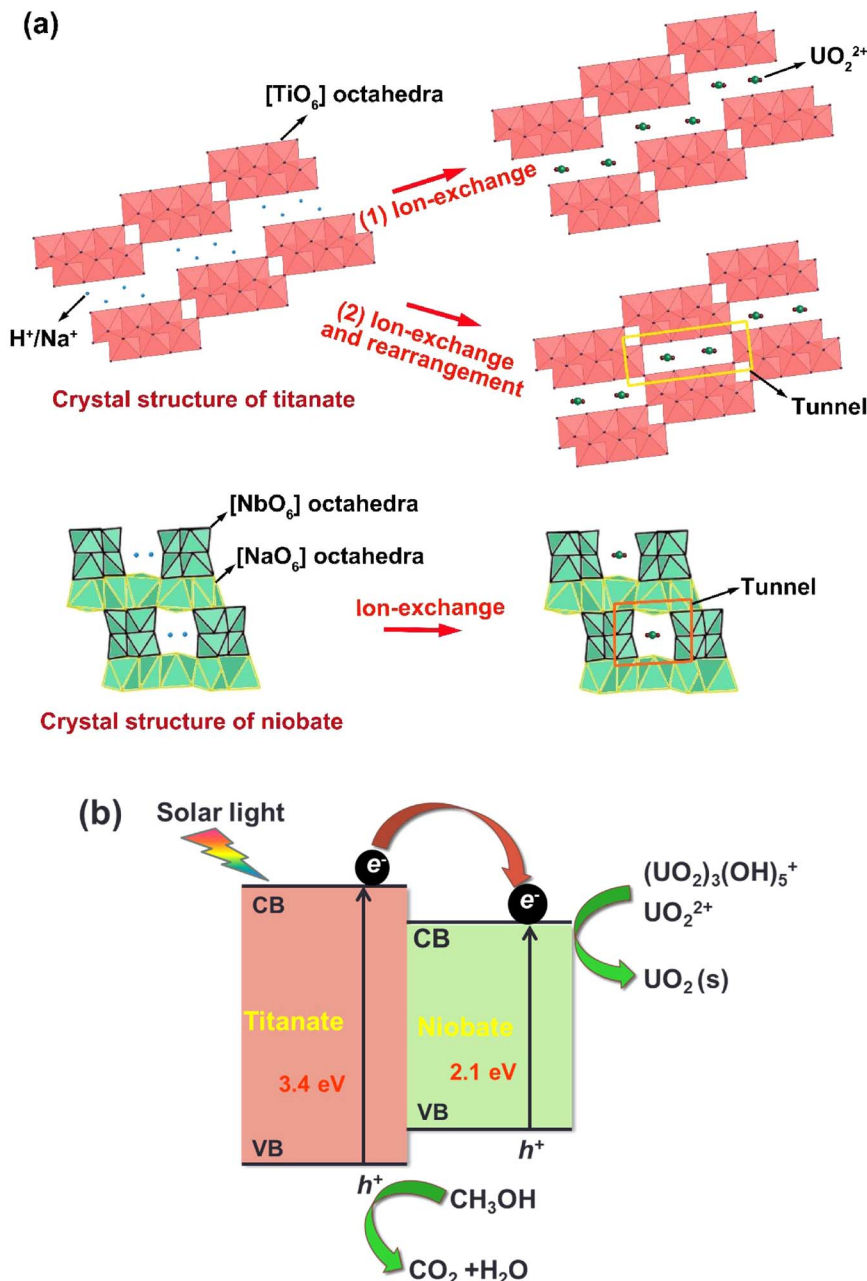


Fig. 7. Schematic representation of (a) adsorption, and (b) photocatalytic reduction of U(VI) by Nb/TiNFs.

than the redox potentials of  $\text{UO}_2^{2+}/\text{UO}_2$  (0.411 V) and  $\text{UO}_2^{2+}/\text{U}^{4+}$  (0.267 V) [24], indicating that reduction of U(VI) is thermodynamically favorable during the photocatalysis (Eqs. 19 and 20). In addition, the potential energy of VB from Nb/TiNFs is more positive than the redox potentials of  $\text{OH}^-/\cdot\text{OH}$  (1.99 V) and  $\text{H}_2\text{O}/\cdot\text{OH}$  (2.37 V) [80–82]. Consequently, the photo-generated holes ( $h^+$ ) can directly oxidize  $\text{OH}^-/\text{H}_2\text{O}$  into  $\cdot\text{OH}$  radicals, and thus, quenching of  $h^+$  by methanol is needed for more efficient U(VI) reduction (Eq. (21)).

DFT calculation on band structure indicates that both sodium titanate and niobate are typical indirect-band-gap semiconductors (Fig. 9a and b) [83]. The theoretical band gaps of titanate and niobate are 3.10 and 2.27 eV, respectively (Table S4), which are close to the reported experimental values [31,44]. The smaller  $E_g$  value (3.10 eV) of titanate than the experimental value (3.42 eV) is due to the known limitation of the plain DFT method [84]. Compared to titanate, narrower band gap energy and more dispersive conduction bands of niobate were observed, suggesting that the photo-generated electrons in niobate possess

a smaller effective mass and a higher migration ability, which then facilitates the photo-reduction reaction for U(VI) (Fig. 7). Figs. 8c and d present the information on the total density of states (TDOS) and partial density of states (PDOS) of titanate and niobate. It is evident that both of the valence band tops of titanate and niobate are constructed from the O 2p orbitals, and they are located at similar energy levels. However, the energy level of the CB bottom in titanate is slightly lower than that in niobate, which is attributed to the variant octahedral ligand field of  $[\text{TiO}_6]$  and  $[\text{NbO}_6]$ . Therefore, the heterojunction architecture of titanate and niobate composite can remedy the low photocatalytic activity of the individual precursor materials. Moreover, the band energy difference facilitates migration of photo-excited electrons from titanate to niobate, thus leading to high photocatalytic activity of the Nb/TiNFs composite.

The survey XPS spectra (Fig. 3a) show that upon U(VI) adsorption, a U 4f peak appeared while the Na 1s peak was notably weakened. This observation provides direct evidence that ion exchange is an important

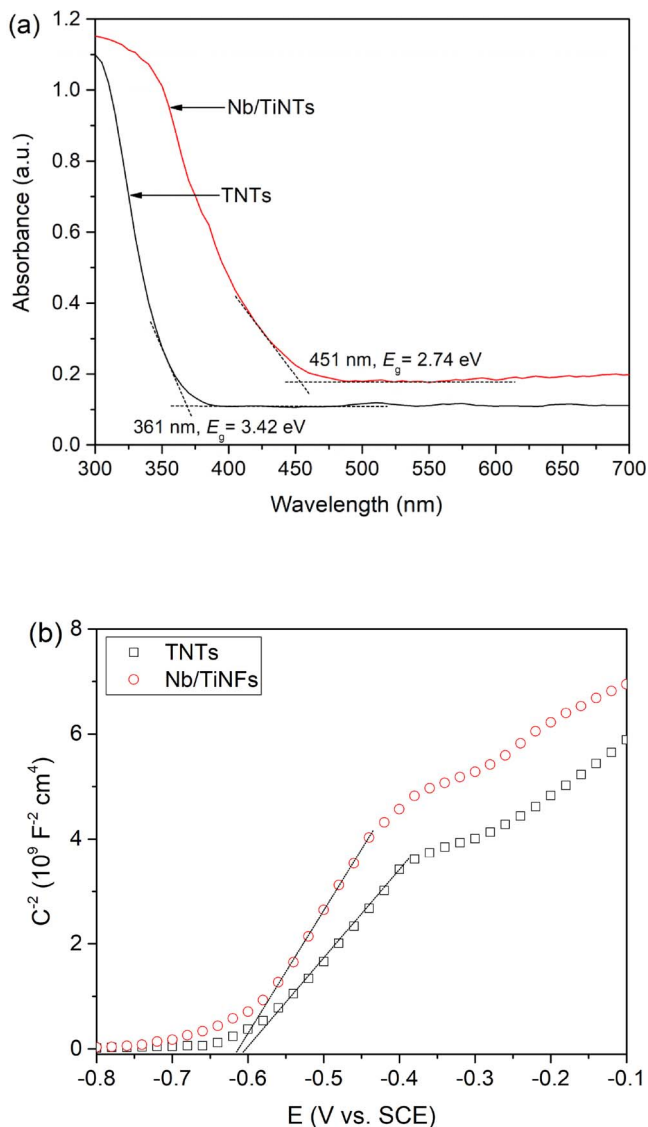


Fig. 8. (a) UV-DRS spectra of TNTs and Nb/TiNFs; (b) Mott-Schottky plots of the TNTs and Nb/TiNFs electrodes vs. SCE.

adsorption mechanism between uranyl cations and inter-layer  $\text{Na}^+$  counter ions. In the high resolution spectra of  $\text{U} 4\text{f}$  (Fig. 3c), the peaks at the binding energy of 392.4 and 381.7 eV belong to the  $\text{U} 4\text{f}_{5/2}$  and  $4\text{f}_{7/2}$  spin states, respectively [12,16,85,86]. The  $\text{U} 4\text{f}_{7/2}$  peak can be further divided into  $\text{U}(\text{VI})$  ( $E_b \approx 381.7 \text{ eV}$ ) and  $\text{U}(\text{VI})$  ( $E_b \approx 380.1 \text{ eV}$ ), respectively [16,85,87]. The results indicate that all adsorbed  $\text{U}$  was in the form of  $\text{U}(\text{VI})$ . However, the atomic percentage of  $\text{U}(\text{IV})$  sharply increased to 59.9 at.% after 2 h of solar irradiation and to 82.8 at.% after 4 h of photolysis, which is consistent with the photo-reduction kinetic results with an initial  $\text{U}(\text{VI})$  concentration of 20 mg/L (Fig. 5). Note the photolysis only modestly increased the total  $\text{U}$  content (from 1.3 to 1.6 at.%, Table 1). In the high resolution spectra of  $\text{O} 1\text{s}$  (Fig. 3b), the peaks at binding energy of 532.3 and 530.0 eV are assigned to  $\text{O}$  from metal bonded surface hydroxyl groups ( $-\text{OH}$ ) and the lattice structure ( $\text{Me}-\text{O}$ , e.g.,  $[\text{TiO}_6]$  and  $[\text{NbO}_6]$ ) [12,45,88]. The increase of  $\text{O}$  percentage in  $-\text{OH}$  from 12.8 at.% to 27.5 at.% after  $\text{U}(\text{VI})$  adsorption results from incorporation of hydroxylated uranyl ions, including  $(\text{UO}_2)_3(\text{OH})_5^+$ ,  $(\text{UO}_2)_2(\text{OH})_2^{2+}$  and  $(\text{UO}_2)_4(\text{OH})_7^+$ , on the surface of Nb/TiNFs, whereas the increase of the lattice  $\text{O}$  from 72.5 at.% to 79.6 at.% (after 2-h photo-reduction) and 83.5 at.% (after 4-h photo-reduction) is due to decomposition of the hydroxylated uranyl ions and formation of  $\text{UO}_2(\text{s})$ .

It is interesting that no immediate re-oxidation of  $\text{U}(\text{IV})$  was found during the photocatalysis process. This observation predicts a rather stable state of the immobilized  $\text{U}(\text{IV})$  species, which can be attributed to: 1) the quenching of  $h^+$  by menthol Eq. (21), 2) the anoxic condition during the photocatalysis, and 3) trapping of uranyl cations and  $\text{UO}_2(\text{s})$  in the tunnel structure of titanate and niobate, which rendered  $\text{U}(\text{VI})$  less desorbable and  $\text{U}(\text{IV})$  less oxidizable due to steric or structural hindrance. The formation of lattice tunnels in titanate-based materials has been widely reported for adsorption of radioactive cations (e.g.,  $\text{Cs}^+$ ) or heavy metal cations (e.g.,  $\text{Hg}^{2+}$ ) [47,89]. Based on our prior work [47], the formation of the tunnel structure of titanate may occur during an adsorption process when both of the following two conditions are satisfied: 1) the target metal cation should have a large ionic radius and can interact with the terminal oxygen atoms in the  $[\text{TiO}_6]$  unit, and 2) the titanate nanomaterial possesses a “metastable” structure, such as titanate nanofibers and titanate nanosheets. The titanate nanoflakes synthesized in this study are a metastable phase of titanate, and the uranyl cations ( $\text{UO}_2^{2+}$  and  $(\text{UO}_2)_3(\text{OH})_5^+$ ) have large ionic radius. As a result, the  $\text{U}(\text{VI})$  species are easily trapped in the lattice tunnels during the adsorption process (Fig. 7a). Likewise, sodium niobate was reported to be subject to the phase deformation, leading to the tunnel structure upon adsorption of radioactive cations, e.g.,  $\text{Sr}^{2+}$  and  $\text{Ba}^{2+}$  [33], which are similar to the  $\text{U}(\text{VI})$  cations in this study (Fig. 7a). The trapping of uranyl cations in the lattice tunnel structures of titanate and niobate along with the subsequent photocatalytic reduction process is of great practical implication as it not only leads to firm immobilization and reduction of  $\text{U}(\text{VI})$ , but also prevent the adsorbed  $\text{U}(\text{VI})$  from being desorbed, and reduced  $\text{U}(\text{IV})$  from being re-oxidized and re-mobilized (see Section 3.5).

The formation of the tunnel structures is also evidenced by the XRD patterns of Nb/TiNFs after  $\text{U}$  adsorption and photocatalysis (Fig. 2), as reflected by the dramatic decrease in the intensity of the titanate interlayer peak ( $20\text{--}10^\circ$ ,  $d_{200}$ ), the shift in the titanate (310) peak ( $2\theta = 28^\circ$ ), disappearance of the titanate peak (110) ( $2\theta = 24^\circ$ ), and vanishing of all the niobate peaks [33,47,89,90]. The XPS data also indicate the ion exchange interaction of uranyl ions with the  $-\text{O}_\text{Na}/\text{H}$  groups, leading to change of the  $[\text{Me}-\text{O}]$  ( $[\text{TiO}_6]$  and  $[\text{NbO}_6]$ ) structures upon  $\text{U}(\text{VI})$  adsorption (Fig. 3b).

### 3.5. Re-oxidation and stability of immobilized $\text{U}$ on Nb/TiNFs

For long-term safe disposal or storage of radionuclides, it is desirable that re-dissolution of the immobilized chemicals is minimized. Fig. 10 presents the concentration histories of re-oxidized  $\text{U}(\text{VI})$  and aqueous  $\text{U}$  when the photo-immobilized  $\text{U}$  was aged under oxic conditions (exposed to air) for 90 days. About 20.5% of  $\text{U}(\text{IV})$  in the solid phase was re-oxidized into  $\text{U}(\text{VI})$  in 90 days, and the re-oxidation mainly occurred in the initial 5 days, indicating that the special tunneling structure of Nb/TiNFs exerts strong shielding effects preventing  $\text{U}(\text{IV})$  from being re-oxidized. It is noteworthy that nearly all (> 97%) of the re-oxidized  $\text{U}(\text{VI})$  remained adsorbed on Nb/TiNFs, with only < 3% being found in the aqueous phase. In the end, 37.8% of immobilized  $\text{U}$  in Nb/TiNFs was in the form of adsorbed  $\text{U}(\text{VI})$  and 62.2% as  $\text{UO}_2(\text{s})$  according to the CARB extraction results. XPS analysis of the  $\text{U}$ -laden Nb/TiNFs after 90 days of aging under oxic conditions further confirmed the high resistance of the solid-phase  $\text{U}(\text{IV})$  to re-oxidation. In the high resolution spectra of  $\text{U} 4\text{f}$  (Fig. S8), 40.5% of  $\text{U}$  was found in the form of  $\text{U}(\text{VI})$ , indicating only 23.3% of  $\text{U}(\text{IV})$  was re-oxidized after 90 days, which is in good agreement with the CARB extraction results. Evidently, both forms of  $\text{U}(\text{VI})$  in the solid phase are highly resistant to desorption or re-dissolution into the aqueous phase.

The nearly irreversible immobilization of  $\text{U}(\text{VI})$  by Nb/TiNFs is in accord with the binding nature as well as the structural effects. For  $\text{U}(\text{VI})$  ions, the strong inner-sphere complexation is further enhanced by the unique lattice tunnel structure of Nb/TiNFs (Fig. 7a). For immobilized  $\text{U}(\text{IV})$ , the slow re-oxidation behavior suggested that its

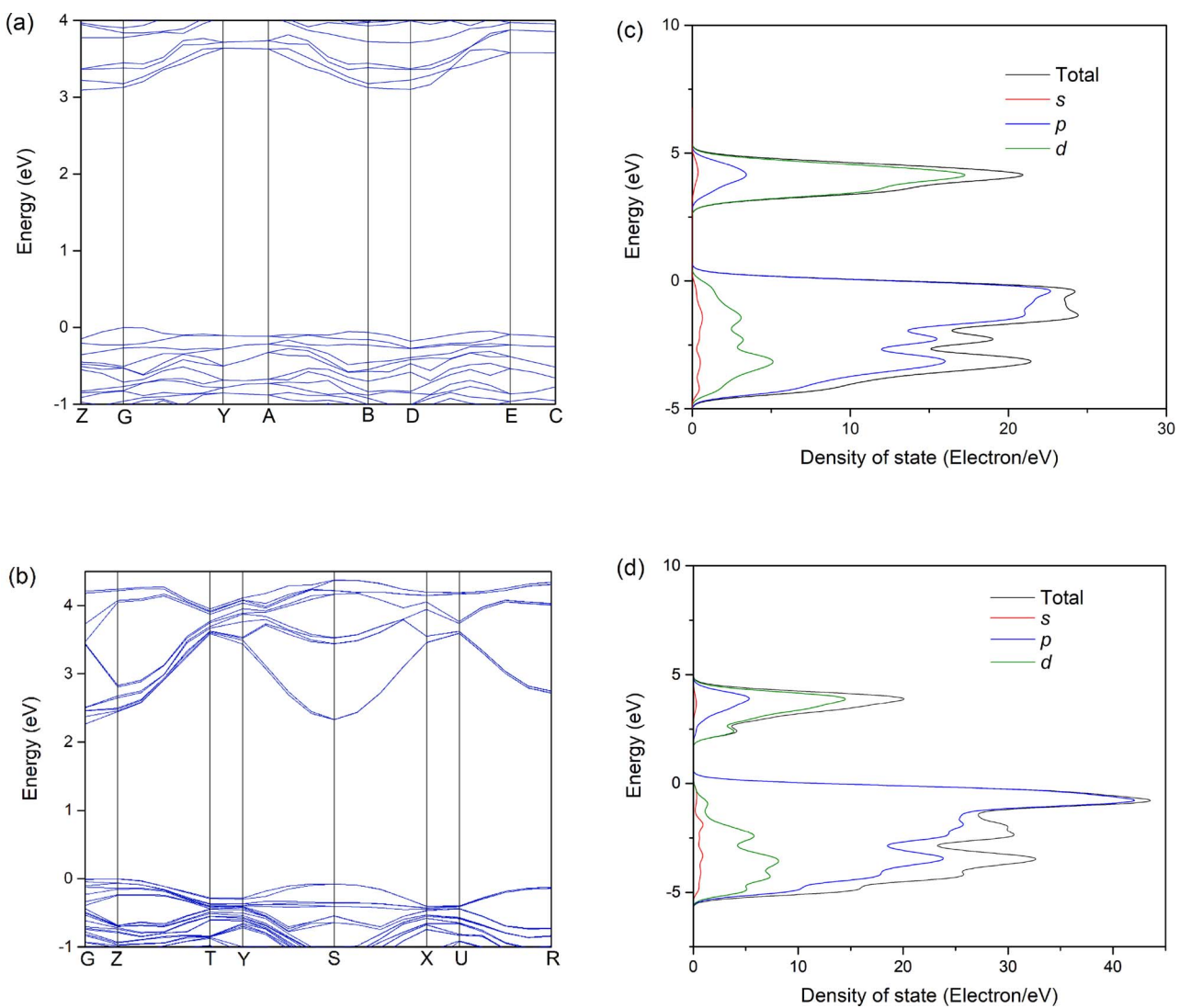


Fig. 9. Calculated band structures of titanate (a) and niobate (b), and the total density of states of titanate (c) and niobate (d).

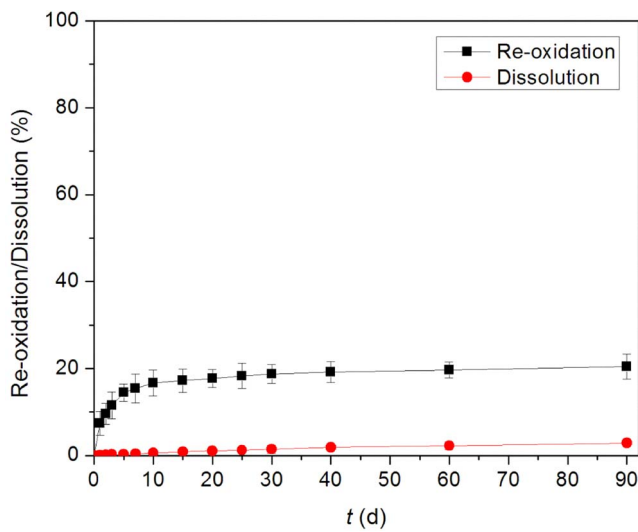


Fig. 10. Re-oxidation of U(IV) and dissolution of immobilized U on Nb/TiNFs during 90 days of exposure to air. Experimental conditions: 0.2 g/L material with ~100 mg/g U(IV) loaded, total suspension volume = 100 mL, solution pH = 5.0, temperature = 25 °C.

sorption was not simply a surface complexation on the external surfaces, but also involved a more intimate association with the internal domains [91]. Zachara et al. [91] observed that the oxidation rate of Tc (IV) precipitated on ferrihydrite was significantly slower than that of neat  $\text{Tc(IV)}_2 \cdot n\text{H}_2\text{O}(s)$ , and they attributed it to the formation of dimeric complexes in the intra-aggregate domains or possibly unoccupied octahedral Fe(III) sites within individual crystallites that were restrictive to oxygen diffusion. Likewise, the intraparticle residence of sorbed/precipitated U(IV) isolated U(IV) from the external oxidizing environment and shielded it from being re-oxidized. It is noteworthy that the precipitated U(IV) and the tunnel lattice effect also set a higher activation energy barrier for the desorption of the adsorbed U(VI) species.

From an application standpoint, it is likely most practical to use Nb/TiNFs for immobilizing high strength U(VI) in contaminated water or nuclear mining drainage. The high adsorption capacity and effective photocatalytic reduction concentrates U(VI) from large volumes of water on a small volume of spent Nb/TiNFs, and the low leachability of immobilized U allows the U-laden material to be safely disposed of or stored.

#### 4. Conclusions

In this study, we reported an innovative niobate tailored titanate

composite nanomaterial, Nb/TiNFs, for successive adsorption and reductive immobilization of U(VI) in contaminated water. The main findings are summarized as follows:

- 1) Nb/TiNFs, with a chemical composition of  $[\text{Na}_2\text{Nb}_2\text{O}_6 \cdot \text{H}_2\text{O}] / 15.9[\text{Na}_{1.6}\text{H}_{0.4}\text{Ti}_3\text{O}_7 \cdot 1.7\text{H}_2\text{O}]$ , were synthesized through a simple one-step hydrothermal method. The composite material exhibited a heterojunction structure of sodium titanate and sodium niobate.
- 2) Nb/TiNFs showed very fast kinetics and high capacity for adsorption of U(VI) due to its easily accessible sites on the nanoflake structure and large specific surface area. The maximum Langmuir adsorption capacity was 298.5 mg/g, which is much higher than conventional adsorbents. The primary adsorption mechanisms for U(VI) species include both ion exchange between uranyl cations and  $\text{Na}^+$  ions in the interlayers of Nb/TiNFs, and inner sphere complexation between U(VI) and the bridging oxygen atoms on titanate.
- 3) Nb/TiNFs were able to facilitate highly efficient photocatalytic reduction of U(VI) under solar light irradiation. More than 89.3% of pre-adsorbed U(VI) was reduced to U(IV) within 4-h photocatalysis at pH 5.0. Acidic conditions were found to favor the integrated adsorption and photocatalytic reduction as pH affects U speciation, surface charge, surface complexation, and photochemical reduction. Almost all the U (99.9%) could be removed at pH 5.0 because of both high adsorption capacity and photocatalytic activity.
- 4) The heterojunction structure of titanate and niobate leads to band gap offset of the composite material, and facilitates the transfer of excited electrons from titanate to niobate, inhibiting recombination of electron-hole pairs, and thus greatly promoting the solar-light-driven photocatalytic activity. UV-DRS and Mott-Schottky analyses indicated a narrowed  $E_g$  of Nb/TiNFs compared to TNTs, and DFT calculation further confirmed the band gap offset of titanate and niobate.
- 5) About 20.5% of immobilized U(IV) on Nb/TiNFs was re-oxidized to U(VI) under oxic conditions over 90 days of exposure to air, and more than 97% of the re-oxidized U(VI) remained adsorbed by Nb/TiNFs. The strong affinity or low leachability of sorbed U is attributed to the strong inner sphere complexation, the tunnel lattice structure, and the intraparticle residence effects, which isolate the immobilized U from being attacked by external environmental gradients such as oxygen and desorbing potential.
- 6) The new composite material provides an energy-effective alternative for treating wastewater contaminated with high strength radionuclides.

## Acknowledgments

Partial financial supports from National Natural Science Foundation of China (Grant No. 41230638, No. 41301232 and No. 51721006) are gratefully acknowledged. H. Liu is grateful to the support by The Doctoral Research Foundation of Taiyuan University of Science and Technology (No. 20152029).

## Appendix A. Supplementary data

Supplementary material related to this article can be found, in the online version, at doi:<https://doi.org/10.1016/j.apcatb.2018.02.062>.

## References

- [1] M. Gavilescu, L.V. Pavel, I. Cretescu, J. Hazard. Mater. 163 (2009) 475–510.
- [2] L.M. Camacho, S. Deng, R.R. Parra, J. Hazard. Mater. 175 (2010) 393–398.
- [3] C. García-Balboa, B. Baselga-Cervera, A. García-Sánchez, J.M. Igual, V. Lopez-Rodas, E. Costas, Aquat. Toxicol. 144 (2013) 116–123.
- [4] S. Massarin, R. Beaudouin, F. Zeman, M. Floriani, R. Gilbin, F. Alonso, A.R. Pery, Environ. Sci. Technol. 45 (2011) 4151–4158.
- [5] J.L. Domingo, Reprod. Toxicol. 15 (2001) 603–609.
- [6] A. Abdelouas, Y. Lu, W. Lutze, H. Nuttall, J. Contam. Hydrol. 35 (1998) 217–233.
- [7] D. Rai, A. Felmy, J. Ryan, Inorg. Chem. 29 (1990) 260–264.
- [8] E.J. O'Loughlin, S.D. Kelly, R.E. Cook, R. Csencsits, K.M. Kemner, Environ. Sci. Technol. 37 (2003) 721–727.
- [9] R. Han, W. Zou, Y. Wang, L. Zhu, J. Environ. Radioact. 93 (2007) 127–143.
- [10] T. Waite, J. Davis, T. Payne, G. Waychunas, N. Xu, Geochim. Cosmochim. Acta 58 (1994) 5465–5478.
- [11] A. Mellah, S. Chegrouche, M. Barkat, J. Colloid Interface Sci. 296 (2006) 434–441.
- [12] W. Liu, X. Zhao, T. Wang, D. Zhao, J. Ni, Chem. Eng. J. 286 (2016) 427–435.
- [13] J.N. Fiedor, W.D. Bostick, R.J. Jarabek, J. Farrell, Environ. Sci. Technol. 32 (1998) 1466–1473.
- [14] Z.J. Li, L. Wang, L.Y. Yuan, C.L. Xiao, L. Mei, L.R. Zheng, J. Zhang, J.H. Yang, Y.L. Zhao, Z.T. Zhu, J. Hazard. Mater. 290 (2015) 26–33.
- [15] B. Hua, B. Deng, Environ. Sci. Technol. 42 (2008) 8703–8708.
- [16] D. Shao, X. Ren, J. Wen, S. Hu, J. Xiong, T. Jiang, X. Wang, X. Wang, J. Hazard. Mater. 302 (2016) 1–9.
- [17] S. Yan, B. Hua, Z. Bao, J. Yang, C. Liu, B. Deng, Environ. Sci. Technol. 44 (2010) 7783–7789.
- [18] X. Zhao, W. Liu, Z. Cai, B. Han, T. Qian, D. Zhao, Water Res. 100 (2016) 245–266.
- [19] W. Liu, S. Tian, X. Zhao, W. Xie, Y. Gong, D. Zhao, Curr. Pollut. Rep. 1 (2015) 280–291.
- [20] J. Chen, D.F. Ollis, W.H. Rulkens, H. Bruning, Colloid. Surf. A 151 (1999) 339–349.
- [21] M.I. Litter, Adv. Chem. Eng. 36 (2009) 37–67.
- [22] E. Liger, L. Charlet, P. Van Cappellen, Geochim. Cosmochim. Acta 63 (1999) 2939–2955.
- [23] Z. Li, Z. Huang, W. Guo, L. Wang, L. Zheng, Z. Chai, W. Shi, Environ. Sci. Technol. (2017).
- [24] C. Lu, P. Zhang, S. Jiang, X. Wu, S. Song, M. Zhu, Z. Lou, Z. Li, F. Liu, Y. Liu, Appl. Catal. B: Environ. 200 (2017) 378–385.
- [25] D.V. Bavykin, J.M. Friedrich, F.C. Walsh, Adv. Mater. 18 (2006) 2807–2824.
- [26] H.H. Ou, S.L. Lo, Sep. Purif. Technol. 58 (2007) 179–191.
- [27] G. Sheng, J. Hu, A. Alsaedi, W. Shammakh, S. Monaquel, F. Ye, H. Li, Y. Huang, A.S. Alshomrani, T. Hayat, J. Mol. Liq. 212 (2015) 563–568.
- [28] L. Yin, P. Wang, T. Wen, S. Yu, X. Wang, T. Hayat, A. Alsaedi, X. Wang, Environ. Pollut. 226 (2017) 125–134.
- [29] F. Yuan, C. Wu, Y. Cai, L. Zhang, J. Wang, L. Chen, X. Wang, S. Yang, S. Wang, Chem. Eng. J. 322 (2017) 125–134.
- [30] Z. Qianqian, B. Tang, H. Guoxin, J. Hazard. Mater. 198 (2011) 78–86.
- [31] W. Liu, X. Zhao, A.G. Borthwick, Y. Wang, J. Ni, ACS Appl. Mater. Interfaces 7 (2015) 19726–19735.
- [32] X. Zhao, Z. Cai, T. Wang, S. O'Reilly, W. Liu, D. Zhao, Appl. Catal. B: Environ. 187 (2016) 134–143.
- [33] J. Sun, L. Liu, X. Zhao, S. Yang, S. Komarneni, D. Yang, RSC Adv. 5 (2015) 75354–75359.
- [34] W. Mu, Q. Yu, X. Li, H. Wei, Y. Jian, J. Alloy. Compd. 693 (2017) 550–557.
- [35] Y. Wang, B.M. Smarsly, I. Djerdj, Chem. Mater. 22 (2010) 6624–6631.
- [36] E. Wada, M. Kitano, K. Yamamoto, K. Nakajima, S. Hayashi, M. Hara, Catal. Sci. Technol. 6 (2016) 4832–4839.
- [37] Q. Chen, W. Zhou, G. Du, L.M. Peng, Adv. Mater. 14 (2002) 1208–1211.
- [38] L. Xiong, Y. Yang, J. Mai, W. Sun, C. Zhang, D. Wei, Q. Chen, J. Ni, Chem. Eng. J. 156 (2010) 313–320.
- [39] S.P. Hyun, J.A. Davis, K. Sun, K.F. Hayes, Environ. Sci. Technol. 46 (2012) 3369–3376.
- [40] M. Kohler, G.P. Curtis, D.E. Meece, J.A. Davis, Environ. Sci. Technol. 38 (2004) 240–247.
- [41] M. Segall, P.J. Lindan, M. Probert, C. Pickard, P.J. Hasnip, S. Clark, M. Payne, J. Phys. Condens. Mat. 14 (2002) 2717.
- [42] J.P. Perdew, K. Burke, M. Ernzerhof, Phys. Rev. Lett. 77 (1996) 3865.
- [43] D. Vanderbilt, Phys. Rev. B 41 (1990) 7892.
- [44] P. Li, S. Ouyang, G. Xi, T. Kako, J. Ye, J. Phys. Chem. C 116 (2012) 7621–7628.
- [45] W. Liu, T. Wang, A.G. Borthwick, Y. Wang, X. Yin, X. Li, J. Ni, Sci. Total Environ. 456 (2013) 171–180.
- [46] W. Liu, J. Ni, X. Yin, Water Res. 53 (2014) 12–25.
- [47] W. Liu, X. Zhao, T. Wang, J. Fu, J. Ni, J. Mater. Chem. A 3 (2015) 17676–17684.
- [48] D.V. Bavykin, V.N. Parmon, A.A. Lapkin, F.C. Walsh, J. Mater. Chem. 14 (2004) 3370–3377.
- [49] S. Zhang, L.M. Peng, Q. Chen, G. Du, G. Dawson, W. Zhou, Phys. Rev. Lett. 91 (2003) 256103.
- [50] X. Sun, Y. Li, Chem. Eur. J. 9 (2003) 2229–2238.
- [51] S. Zhang, Q. Chen, L.M. Peng, Phys. Rev. B 71 (2005) 014104.
- [52] H. Xu, M. Nyman, T.M. Nenoff, A. Navrotsky, Chem. Mater. 16 (2004) 2034–2040.
- [53] W. Liu, P. Zhang, A.G. Borthwick, H. Chen, J. Ni, J. Colloid Interface Sci. 423 (2014) 67–75.
- [54] W. Liu, W. Sun, Y. Han, M. Ahmad, J. Ni, Colloid. Surf. A 452 (2014) 138–147.
- [55] S. Brunauer, L.S. Deming, W.E. Deming, E. Teller, J. Am. Chem. Soc. 62 (1940) 1723–1732.
- [56] M. Thommes, K. Kaneko, A.V. Neimark, J.P. Olivier, F. Rodriguez-Reinoso, J. Rouquerol, K.S. Sing, Pure Appl. Chem. 87 (2015) 1051–1069.
- [57] X. Li, W. Zhang, W. Cui, Y. Sun, G. Jiang, Y. Zhang, H. Huang, F. Dong, Appl. Catal. B: Environ. 221 (2018) 482–489.
- [58] J. Yu, C.Y. Jimmy, M.K.-P. Leung, W. Ho, B. Cheng, X. Zhao, J. Zhao, J. Catal. 217 (2003) 69–78.
- [59] A. Turki, H. Kochkar, C. Guillard, G. Berhault, A. Ghorbel, Appl. Catal. B: Environ. 138 (2013) 401–415.
- [60] Y.S. Ho, G. McKay, Chem. Eng. J. 70 (1998) 115–124.
- [61] Y.S. Ho, G. McKay, Process Biochem. 34 (1999) 451–465.
- [62] I. Langmuir, J. Am. Chem. Soc. 40 (1918) 1361–1403.

[63] H. Freundlich, Z. Phys. Chem. 57 (1906) 385–470.

[64] K. Hall, L. Eagleton, A. Acrivos, T. Vermeulen, Ind. Eng. Chem. Fund. 5 (1966) 212–223.

[65] C. Kütahyalı, M. Eral, Sep. Purif. Technol. 40 (2004) 109–114.

[66] M. Sprynsky, T. Kowalkowski, H. Tutu, E.M. Cukrowska, B. Buszewski, Chem. Eng. J. 171 (2011) 1185–1193.

[67] Y. Sun, J. Li, X. Wang, Geochim. Cosmochim. Acta 140 (2014) 621–643.

[68] Y. Sun, S. Yang, Y. Chen, C. Ding, W. Cheng, X. Wang, Environ. Sci. Technol. 49 (2015) 4255–4262.

[69] R. Hu, D. Shao, X. Wang, Polym. Chem. 5 (2014) 6207–6215.

[70] H. Al-Ekabi, N. Serpone, J. Phys. Chem. 92 (1988) 5726–5731.

[71] J. Yu, H. Yu, B. Cheng, C. Trapalis, J. Mol. Catal. A: Chem. 249 (2006) 135–142.

[72] X. Zhao, P. Du, Z. Cai, T. Wang, J. Fu, W. Liu, Environ. Pollut. 232 (2018) 580–590.

[73] M.J. Comarmond, T.E. Payne, J.J. Harrison, S. Thiruvoth, H.K. Wong, R.D. Augherson, G.R. Lumpkin, K. Müller, H. Foerstendorf, Environ. Sci. Technol. 45 (2011) 5536–5542.

[74] J. Vandenborre, R. Drot, E. Simoni, Inorg. Chem. 46 (2007) 1291–1296.

[75] E. Sylwester, E. Hudson, P. Allen, Geochim. Cosmochim. Acta 64 (2000) 2431–2438.

[76] A. Singh, J.G. Catalano, K.U. Ulrich, D.E. Giammar, Environ. Sci. Technol. 46 (2012) 6594–6603.

[77] M. Wazne, G.P. Korfiatis, X. Meng, Environ. Sci. Technol. 37 (2003) 3619–3624.

[78] K. Gelderman, L. Lee, S. Donne, J. Chem. Edu. 84 (2007) 685.

[79] H. Huang, D. Li, Q. Lin, Y. Shao, W. Chen, Y. Hu, Y. Chen, X. Fu, J. Phys. Chem. C 113 (2009) 14264–14269.

[80] A. Bard, Standard Potentials in Aqueous Solution, Routledge, 2017.

[81] W. Cui, J. Li, F. Dong, Y. Sun, G. Jiang, W. Cen, S.C. Lee, Z. Wu, Environ. Sci. Technol. 51 (2017) 10682–10690.

[82] J. Li, Xa. Dong, Y. Sun, W. Cen, F. Dong, Appl. Catal. B: Environ. 226 (2018) 269–277.

[83] M.S. Hybertsen, S.G. Louie, Phys. Rev. Lett. 55 (1985) 1418.

[84] W. Cui, J. Li, W. Cen, Y. Sun, S. Lee, F. Dong, J. Catal. 352 (2017) 351–360.

[85] Y.K. Kim, S. Lee, J. Ryu, H. Park, Appl. Catal. B: Environ. 163 (2015) 584–590.

[86] G. Sheng, P. Yang, Y. Tang, Q. Hu, H. Li, X. Ren, B. Hu, X. Wang, Y. Huang, Appl. Catal. B: Environ. 193 (2016) 189–197.

[87] D. Shao, G. Hou, J. Li, T. Wen, X. Ren, X. Wang, Chem. Eng. J. 255 (2014) 604–612.

[88] H.H. Ou, C.H. Liao, Y.H. Liou, J.H. Hong, S.L. Lo, Environ. Sci. Technol. 42 (2008) 4507–4512.

[89] D. Yang, S. Sarina, H. Zhu, H. Liu, Z. Zheng, M. Xie, S.V. Smith, S. Komarneni, Angew. Chem. Inter. Ed. 50 (2011) 10594–10598.

[90] X.D. Meng, D.Z. Wang, J.H. Liu, S.Y. Zhang, Mater. Res. Bull. 39 (2004) 2163–2170.

[91] J.M. Zachara, S.M. Heald, B.H. Jeon, R.K. Kukkadapu, C. Liu, J.P. McKinley, A.C. Dohnalkova, D.A. Moore, Geochim. Cosmochim. Acta 71 (2007) 2137–2157.